8-band k.p modelling of mid-infrared intersubband absorption in Ge quantum wells

D. J. Paul[1, a)]
University of Glasgow, School of Engineering, Rankine Building, Oakfield Avenue, Glasgow, G12 8LT, U.K.

(Dated: 9 July 2016)

The 8-band **k**.**p** parameters which include the direct band coupling between the conduction and the valence bands are derived and used to model optical intersubband transitions in Ge quantum well heterostructure material grown on Si substrates. Whilst for Si rich quantum wells the coupling between the conduction bands and valence bands is not important for accurate modelling, the present work demonstrates that the inclusion of such coupling is essential to accurately determine intersubband transitions between hole states in Ge and Ge-rich $Si_{1-x}Ge_x$ quantum wells. This is due to the direct bandgap being far smaller in energy in Ge compared to Si. Compositional bowing parameters for a range of the key modelling input parameters required for Ge/SiGe heterostructures including the Kane matrix elements, the effective mass of the $\Gamma_{2'}$ conduction band and the Dresselhaus parameters for both 6-band and 8-band **k**.**p** modelling have been determined. These have been used to understand valence band intersubband transitions in a range of Ge quantum well intersubband photodetector devices in the mid-infrared wavelength range.

PACS numbers: 78.20.Ci, 71.20.-b, 07.57.Kp
Keywords: bandstructure, Ge quantum wells, intersubband absorption

I. INTRODUCTION

There are many applications in the mid-infrared part of the electromagnetic spectrum which include thermal imaging[1] and the unique identification of molecules through absorption spectroscopy.[2] For all these applications, sources of mid-infrared light and photodetectors[1,3] are key to enable any application. III-V and II-VI semiconductor materials have dominated over the last decades with both interband and intersubband emission and/or absorption devices[1,3,4] but there is now significant interest in developing technology on silicon substrates[5–7] to enable far cheaper systems for mass market applications in environmental sensing, personalised healthcare and security.[2,8] SiGe quantum well (QW) intersubband photodetectors (QWIPs) have previously been demonstrated[9–11] but the number of QWs was limited by the SiGe critical thickness thereby limiting performance. Now Ge QWs have the potential to improve this performance significantly in the mid-infrared and the number of QWs can be increased using strain symmetrisation of the QWs and barriers to allow improved absorption in the longer wavelength mid-infrared.[6,12]

The key to understanding the physics behind mid-infrared intersubband device operation and designing optimized devices is a band structure tool that can accurately calculate the bands, subbands and matrix elements to allow the optical absorption and emission to be calculated. A wide range of tools have been used to calculate the band structures of Si/SiGe and Ge/SiGe including pseudopotential[13,14], tight binding[15] and **k**.**p**-theory tools.[16–18] Some of these tools require significant computational resources to model even simple structures. **k**.**p** method tools are more practical as they can be used on desktop or laptop computers and do not require access to significant computational resource. For intersubband absorption in SiGe QWs, a range of 6-band **k**.**p** tools have demonstrated good agreement with experimental results in both the mid-infrared[19–21] and the far-infrared (THz) regimes[18,22–24]. Key to this accuracy are the input parameters and also the level of bowing of many of the parameters for compositional changes as simple linear extrapolations between the Si and Ge parameters does not always provide accurate modelling.

Previous work using an 8-band **k**.**p** tool available as Nextnano with scaled 6-band **k**.**p** parameters was sufficient to allow the interband optical absortption for Ge QW quantum confined Stark effect modulators to be determined.[18] This approach, however, when used provided poor agreement with experimental results for intersubband absorption for Ge-rich heterolayers[7] as it does not accurately account for the direct bandgap coupling between the Γ-valley and the valence bands. Interband coupling is far more important for materials with smaller bandgaps hence the direct band coupling effects are far stronger for Ge and Ge-rich materials compared to Si. This has previously been determined to be important for accurate band structure calculations for cyclotron resonance measurements of Ge QWs[25] where the Γ-valley is only 140 meV above the L-valley conduction band edge.[26] Winkler et al.[25] used the approach of Lawaetz[27] to derive 6-band Luttinger parameters which included coupling between the Γ-valley and the hole bands in addition to the bowing parameters cover the whole compositional range from Si to Ge.

In this paper, a similar approach is used to Win-

a)Electronic mail: Douglas.Paul@glasgow.ac.uk

kler et al.[25], using the compositional scaling defined by Lawaetz[27] to calculate the 6-band **k.p** Luttinger and Dresselhaus parameters including the bowing of these parameters with Ge composition, x where the direct band coupling between the conduction and the valence bands is explicitly included. More recent experimental data especially in Ge-rich heterostructures is also used to improve the accuracy of a number of the input parameters used in the modelling and to also derive appropriate bowing parameters where required. The 8-band **k.p** parameters are then derived and used in the Nextnano++ tool[28–30] to accurately model mid-infrared intersubband absorption for a range of designs. Finally the optical transitions as a function of QW width will be calculated over a wide range of thicknesses. The work demonstrates the importance of coupling between the valence and conduction bands for calculating optical matrix elements and transitions for intersubband transitions in Ge and Ge-rich QWs.

II. TEMPERATURE DEPENDENCE AND BOWING

Bowing parameters have been introduced to allow a single parameter to account for any non-linear bowing of the value of any physical, electrical or optical parameter in alloyed semiconductor materials over the complete compositional range. In this paper, bowing parameters, $B_{Si_{1-x}Ge_x}$ for a composition x of $Si_{1-x}Ge_x$ are used to account for any non-linear variance of a parameter from the linearly extrapolated Si and Ge values as

$$\chi_{Si_{1-x}Ge_x} = x\chi_{Ge} + (1-x)\chi_{Si} - x(1-x)B_{Si_{1-x}Ge_x} \quad (1)$$

where χ_{Si}, χ_{Ge} and $\chi_{Si_{1-x}Ge_x}$ are the values of the given parameter for the materials Si, Ge and $Si_{1-x}Ge_x$ respectively. Not all the parameters required for the band structure calculations do require bowing parameters. The lattice constant, $a(x)$ is well known from the original x-ray diffraction data of Dismukes et al.[32] to require a bowing parameter which is presented in Table I. As will be demonstrated later, a single bowing parameter cannot always account for the variation of a parameter as a function of the Ge composition and more complicated variations with the Ge composition, x are required.

The temperature dependence of the bandgap used the approach of Varshni[33] who defined the temperature dependence of the bandgaps as

$$E_g^i(T) = E_g^i(0K) - \frac{\alpha^i}{T + \beta^i} \quad (2)$$

where i = Γ, L or Δ dependent on which conduction band valley is being considered. The Varshni parameters used in this work are presented in Table I.

To enable coupling between the conduction and valence bands to be calculated later in the paper, the energy gaps between a number of different bands in both Si and Ge are required and are presented in Table I. In this paper, E_g is defined as the minimum bandgap between the lowest conduction band edge and the highest valence band edge which swaps from a Δ-band to valence band to the L-bands to valence bands at a Ge content of approximately $x = 0.85$.[12] Bowing parameters for the Δ-valley transitions to the valence band have been extracted from photoluminescence.[35] E_0 is defined as the energy difference between the $\Gamma_{25'}$ and $\Gamma_{2'}$ bands (the fundamental p-s bonding orbitals energy gap) and E_0' is defined as the energy difference between the $\Gamma_{25'}$ and Γ_{15} bands (the p-p bonding orbitals energy gap).

III. 6-BAND k.p PARAMETERS AND COUPLING

There are a number of different sets of material parameters required for 6-band and 8-band **k.p** which can be separated into the three main approaches of Dresselhaus[40], Luttinger[41] and Foreman.[42,43] A complete review of all these parameters and how these parameters are related has been provided by Birner.[30] The Nextnano++ tool requires Dresselhaus parameters for both the 6-band and 8-band **k.p** tools. A detailed review of the required parameters can be found in refs. 28 and 29.

Coupling between the conduction bands and the valence bands is introduced using the Kane momentum matrix elements

$$E_p = \frac{2}{m_0} |\langle X|P_y|\Gamma_2'\rangle|^2 = \frac{2m_0}{\hbar^2}P^2 \quad (3)$$

$$E_p' = \frac{2}{m_0} |\langle X|P_y|\Gamma_{15}\rangle|^2 \quad (4)$$

where $|X\rangle$ is the yz-type wave function of the Γ_{25}' valence-band states in the case where spin-orbit scattering is neglected. The values for Si and Ge used in this work are presented in Table III. P is defined as the Kane parameter and the values for materials are frequently quoted using P rather than the E_p. F is another key parameter for the coupling and is defined as the first Kane momentum matrix element divided by the direct bandgap

$$F = \frac{E_p}{E_0} \quad \text{and} \quad F' = \frac{E_p'}{E_0} \quad (5)$$

Using the scaling approach of Lawaetz[27] for analysing a range of semiconductors using **k.p**-theory, the variation of a number of the **k.p**-parameters over the whole Ge composition x can be described using

$$\delta(x) = [1 + 1.23(D(x) - 1)] \left(\frac{a_{Si}}{a(x)}\right)^2 \quad (6)$$

TABLE I. The input parameters used in the 8-band **k.p** modeling with bowing parameters where used.

Parameter	Silicon	Germanium	$Si_{1-x}Ge_x$ Bowing
Lattice constant, a (nm)	0.543102[a]	0.5679[a]	0.0026174[b]
Elastic constant, c_{11} (GPa)	165.77[c]	128.53[c]	
Elastic constant, c_{12} (GPa)	63.93[c]	48.28[c]	
Elastic constant, c_{44} (GPa)	79.62[c]	66.80[c]	
Varshni α_Γ (meV/K)	536.7[d]	684.2[d]	
Varshni β_Γ (K)	745.8[d]	398[d]	
Varshni α_L (meV/K)	536.7[d]	456.1[d]	
Varshni β_L (K)	745.8[d]	210[d]	
Varshni α_Δ (meV/K)	702.1[d]	477.4[d]	
Varshni β_Δ (K)	1108[d]	235[d]	
E_0 ($\Gamma_{25'} \rightarrow \Gamma_{2'}$ eV)	4.18510 (at 4.2 K)[c]	0.8981 (at 1.5 K)[d]	
E_0' ($\Gamma_{25'} \rightarrow \Gamma_{15}$ eV)	3.40[e]	3.124 (at 1.5 K)[c]	
E_g (Δ eV)	1.17 (at 0 K)[a]	0.931[f]	0.206[f]
E_g (L eV)	2.01[f]	0.785 (at 0 K)[c]	
Δ_{SO} (meV)	44[c]	289[c]	
$\epsilon(0)$	11.9[c]	16.0[c]	

[a] Reference[31]
[b] Reference[32]
[c] Reference[26]
[d] Reference[33]
[e] Reference[34]
[f] Reference[35]

TABLE II. The deformation potentials for Si and Ge.

Parameter	Silicon	Germanium
a_v (eV)	1.80[g]	1.24[g]
b (eV)	-2.10[h]	-2.86[i]
d (eV)	-4.85[h]	-5.28[i]
a_c^Γ (eV)	-10.39[j]	-10.41[j]
a_c^L (eV)	-0.66[k]	-1.54[k]
a_c^X (eV)	3.3[l]	2.55[k]
Ξ_u^Γ	0.0	0.0
Ξ_u^L	16.14[k]	16.2[m]
Ξ_u^Δ	8.6[h]	9.42[k]

[g] Reference[34]
[h] Reference[36]
[i] Reference[37]
[j] Reference[38]
[k] Reference[39]

where the change as a function of composition is inversely related to the square of the bowing of the lattice constant, $a(x)$ relative to the lattice constant of Si, a_{Si}. For example the first Kane matrix element can be redefined as

$$E_p = E_p(Si)\delta(x) \tag{7}$$

as a function of the Ge composition, x. Here $D(x)$ is defined by Van Vechten[44] as

$$D(x) = \frac{N_{eff}}{N} \tag{8}$$

where N is the number of carriers (= number of electrons per two-atom unit cell). This term is to account for the d electron effects in Ge. N_{eff} is the effective concentration of valence electrons and is obtained from the low frequency dielectric constant , $\epsilon(0)$ in the Penn model through

$$N_{eff} = \frac{m_0 E_g^2}{q^2\hbar^2}(\epsilon(0) - 1) \tag{9}$$

where q is the absolute value of the charge of an electron, $\hbar$ is Planck's constant divided by 2π and m_0 is the mass of an electron. The Penn model accounts for the scaling of the average electronic bandgap as a power function of the lattice constant in non-polar materials. For elements without any d electrons such as Si, $N_{eff} = N$ where N accounts for eight electrons per diatomic volume.[27]

The bowing of the direct E_0' transition used the approach of Van Vechten[44] of linking this to the bowing of the lattice parameter as a function of composition, x as

$$E_0' = E_0'(Si)\left(\frac{a(x)}{a_{Si}}\right)^{-2.08} \tag{10}$$

but to accurately fit this equation to the data in Table I for Ge, the exponent was increased to -2.08 for this work.

The bowing of the Luttinger parameters γ_1, γ_2, γ_3 and κ with the Ge composition, x was suggested by Winkler et al.[25] to be

$$\gamma_1 = \frac{1}{3}\frac{E_p}{E_0} + \frac{2}{3}\frac{E_p'}{E_0'} + \overline{\gamma_1} \tag{11}$$

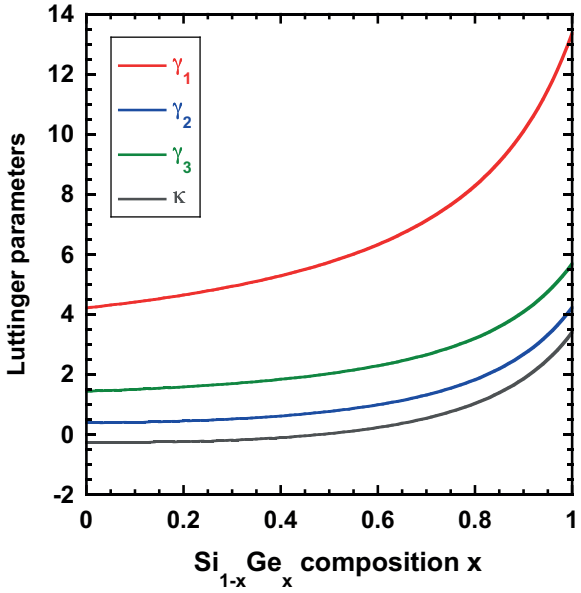

FIG. 1. The calculated Luttinger parameters for 6-band **k.p** modelling which demonstrate a strong bowing as a function of Ge content, x.

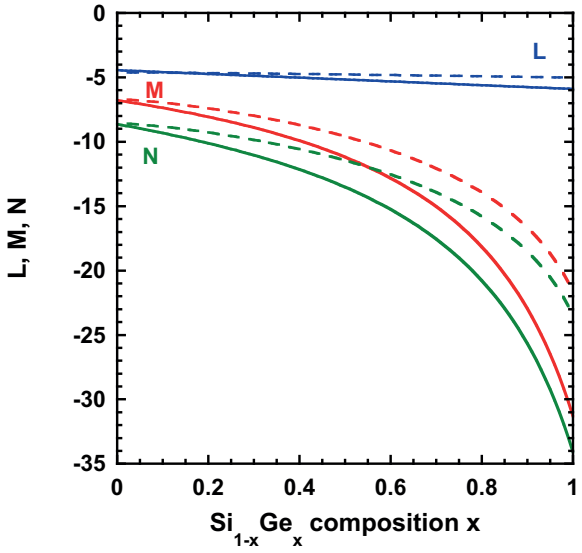

FIG. 2. Solid lines: the calculated 6-band **k.p** Dresselhaus parameters in this work which demonstrate a strong bowing with Ge content, x. Dashed lines: the 6-band **k.p** Dresselhaus parameters from Rieger and Vogl which also produce strong bowing of the parameters as a function of Ge content, x.[13]

.

$$\gamma_2 = \frac{1}{6}\frac{E_p}{E_0} - \frac{1}{6}\frac{E'_p}{E'_0} + \overline{\gamma_2} \tag{12}$$

$$\gamma_3 = \frac{1}{6}\frac{E_p}{E_0} + \frac{1}{6}\frac{E'_p}{E'_0} + \overline{\gamma_3} \tag{13}$$

$$\kappa = \frac{1}{6}\frac{E_p}{E_0} - \frac{1}{6}\frac{E'_p}{E'_0} + \overline{\kappa} \tag{14}$$

The values of $\overline{\gamma_1}$, $\overline{\gamma_2}$, $\overline{\gamma_3}$ and $\overline{\kappa}$ are the linearly interpolated values between the bulk Si and Ge values of the γ and κ parameters.

The Luttinger parameters as calculated by equations 11 to 14 are plotted in Fig. 1 and demonstrate strong bowing as a function of Ge content, x. It should be stated that the Luttinger parameters for Si and Ge using the approach agree with the experimental values in Fig. 1. The intermediate values for different Ge compositions have not been tested for all the compositions with bulk material but as will be demonstrated later, the agreement to a range of experiments which include $Si_{0.5}Ge_{0.5}$ and $Si_{0.2}Ge_{0.8}$ suggest that bowing parameters obtained from Fig. 1 (see Table III) are not unreasonable.

The Luttinger parameters can be converted into the Dresselhaus parameters[30] using

$$L = (-\gamma_1 - 4\gamma_2 - 1)\frac{\hbar^2}{2m_0} \tag{15}$$

$$M = (2\gamma_2 - \gamma_1 - 1)\frac{\hbar^2}{2m_0} \tag{16}$$

$$N = (-6\gamma_3)\frac{\hbar^2}{2m_0} \tag{17}$$

The 6-band Dresselhaus parameters as calculated from equations 15 to 17 are plotted in Fig. 2 and demonstrate strong bowing of the parameters as a function of Ge content, x. Numerical fits have been applied to these Dresselhaus parameters to obtain bowing parameters. Whilst a single bowing parameter was obtained for M, both L and N required quadratic bowing parameters as a function of the Ge composition as presented in Table III. Also plotted in Fig. 2 with dashed lines for comparison are the Dresselhaus parameters calculated by Rieger and Vogl.[13]. Whilst the Rieger and Vogl parameters are accurate for pure Si, it was noted in the publication that they underestimated the absolute value of the Dresselhaus parameters for Ge, at least for the values obtained through cyclotron resonance from ref. 45 as used in the present work (see Table III). The solid lines in Fig. 2 accurately produce the experimental values for pure Si and Ge heterolayers but the values for intermediate Ge compositions, x are not available from experiments to allow accurate bowing parameters to be determined directly. It should be noted that the bowing parameters for L and N correspond to significant deviations beyond quadratic behaviour.

IV. 8-BAND k.p PARAMETERS

There are five main parameters for 8-band **k.p** modeling.[30] Before these parameters can be calculated the conduction band effective mass for Γ'_2 is required. Using the approximation of Cardona[46] this can be calculated as

TABLE III. The input parameters used in the 6-band **k.p** modeling.

Parameter	Silicon	Germanium	$Si_{1-x}Ge_x$ Bowing
Kane matrix element, E_p (eV)	21.6[k]	26.3[k]	-0.57058
Kane matrix element, E_p' (eV)	14.4[k]	17.5[k]	
γ_1	4.22[k]	13.38 ± 0.02[l]	equation (11)
γ_2	0.39[k]	4.25 ± 0.04[l]	equation (12)
γ_3	1.44[k]	5.69 ± 0.03[l]	equation (13)
κ	-0.26[a]	3.41[a]	$4.0671 - 3.4945x + 11.464x^2$
L ($\frac{\hbar^2}{2m_L^*}$)	-6.78[j]	-31.3 ± 0.35[l]	$-24.485 + 21.271x - 69.237x^2$
M ($\frac{\hbar^2}{2m_M^*}$)	-4.44[j]	-5.90 ± 0.05[l]	-0.0061083
N ($\frac{\hbar^2}{2m^*}$)	-8.64[j]	-34.1 ± 0.18[l]	$-24.476 + 21.211x - 69.146x^2$

[j] Reference[13]
[k] Reference[27]
[l] Reference[45]

$$\frac{m_0}{m_c^*(\Gamma_2')} = 1 - F(1 - \frac{\Delta_{SO}}{3(E_0 + \Delta_{SO})}) + F' \qquad (18)$$

where Δ_{SO} is the split-off energy and Lawaetz[27] estimated that $F' = -2$. The values determined using the data in the present work are 0.241 m_0 for Si and 0.0383 m_0 for Ge. The experimental determined value for Ge is 0.038 m_0 at 300 K[26] so the calculated value being used is extremely close to the experimental value providing some confidence in the approach. No values for Si are available to provide any comparison between the model and experiment as the lowest direct conduction band at the Γ-point is over 2 eV above the conduction band edge. The values for all Ge compositions, x were also calculated which required the fitting of a bowing parameter of 0.077135 to allow an analytical calculation of the values for all $Si_{1-x}Ge_x$ compositions.

The S parameter has been introduced into 8-band **k.p**-theory modelling to add coupling between the lowest direct conduction band and the highest valence band in energy.[47] It is calculated using

$$S = \frac{m_0}{m_c^*(\Gamma_2')} - E_p \frac{E_0 + \frac{2}{3}\Delta_{SO}}{E_0(E_0 + \Delta_{SO})} \qquad (19)$$

For both Si and Ge the calculated values are -1.0 as demonstrated in Table IV. The coupling can be turned off by setting the Kane parameter, E_p to zero. The inversion asymmetry parameter, B was define by Loehr.[48] B is zero for crystals which have inversion symmetry such as those with a diamond lattice structure and so $B = 0$ for both Si and Ge. It has been assumed that $B = 0$ for all $Si_{1-x}Ge_x$ alloys even though the random alloys will not have inversion symmetry.

The 8-band Dresselhaus parameters L', M' and N' can now be calculated and are defined as[30]

$$L' = L + \frac{E_p}{E_0} \qquad (20)$$

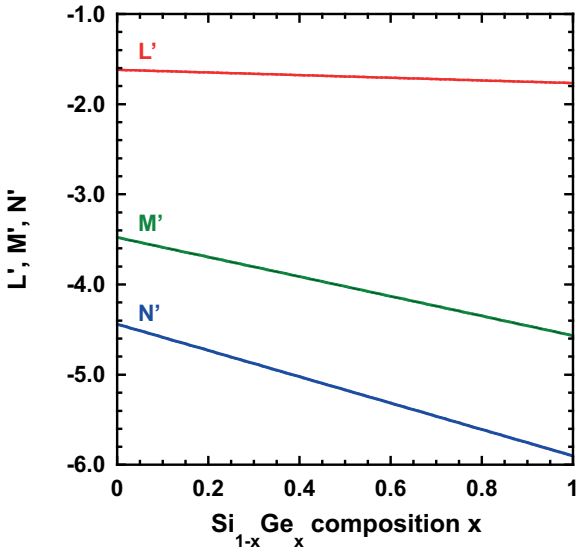

FIG. 3. Solid lines: the calculated 8-band **k.p** Dresselhaus parameters which demonstrate negligible bowing below 0.18 % of a linear fit to the data for the Ge content, x.

.

$$M' = M \qquad (21)$$

$$N' = N + \frac{E_p}{E_0} \qquad (22)$$

Table IV lists all the required 8-band **k.p**-theory parameters as derived from the 6-band **k.p** parameters in Table III. Figure **??** plots the 8-band Dresselhaus parameters and includes the bowing of the parameters which are presented in Table IV. The L' parameter is completely linear. It is clear that the bowing of all the 8-band Dresselhaus parameters are small compared to the 6-band Dresselhaus parameters and a linear fit provides uncertainties for all values of Ge content less than 0.18% of the bowed values. This is to be expected as the 8-band parameters include the direct bandgap coupling.

TABLE IV. The input parameters used in the 8-band **k.p** modeling and the Dresselhaus parameters derived in this work including the bowing parameters.

Parameter	Silicon	Germanium	$Si_{1-x}Ge_x$ Bowing
S (eV)	-1.0	-1.0	
B	0[a]	0[a]	
$m_c^*(\Gamma_{2'})$ (m_0)	0.241	0.0383	0.077135
L' $(\frac{\hbar^2}{2m_2^*})$	-1.62	-1.77	
M' $(\frac{\hbar^2}{2m_3^*})$	-4.44	-4.93	-0.0061083
N' $(\frac{\hbar^2}{2m^*})$	-3.48	-4.57	-0.0061083

[a] Reference[26]

V. MID-INFRARED INTERSUBBAND OPTICAL TRANSITIONS

The experimental results for mid-infrared intersubband transitions that are modelled in this paper were published in Gallacher et al..[7] The material consisted of 500 periods of strain symmetrized[6] Ge QWs with $Si_{0.5}Ge_{0.5}$ barriers all grown on relaxed $Si_{0.2}Ge_{0.8}$ virtual substrates on top of Si (001) substrates. The $Si_{0.5}Ge_{0.5}$ barriers were doped p-type using boron at 2×10^{18} cm^{-3} whilst the Ge QWs were nominally undoped. Three different QW widths were measured by Fourier transform infrared spectroscopy (FTIR) with the barriers also scaled to keep the total structures strain symmetrized.[6,12]

For intersubband transitions, heavy hole (HH) to HH and light hole (LH) to LH produce only z-polarised absorption in the parabolic band approximation and HH to LH transitions produce both xy-polarised and z-polarised absorption.[6,22–24] Non-parabolicity due to the mixing of subband states for $k_{\|} \neq 0$ can relax these selection rules allowing some xy-polarised absorption from HH to HH and LH to LH transitions. The measurement geometry in ref. 7 was surface normal so only xy-polarised absorption is expected for the parabolic approximation but dependent on the samples, non-parabolicity, scattering from heterointerfaces and scattering from the substrate can also allow a smaller amount of z-polarized transitions to be observed even in this surface-normal geometry.[49,50]

The transmission electron microscope (TEM) measurements of the narrowest Ge QW found that the samples consisted of a 5.4 ± 0.4 nm Ge QW with $Si_{0.5}Ge_{0.5}$ barriers all strain symmetrized to a $Si_{0.2}Ge_{0.8}$ relaxed buffer. Figure 4 compares the absorption data measured in surface-normal (xy-polarized) by Fourier transform infrared (FTIR) spectrometry[7] with solutions to the present 8-band **k.p** modelling. To get the model to fit the experiments, the Ge QW was set at 5.2 nm and the $Si_{0.5}Ge_{0.5}$ barriers to 3.5 nm which are both well within the uncertainty of the TEM measurements.[7] Whilst only the $Si_{0.5}Ge_{0.5}$ barriers are doped, the majority of the carriers fall into the QWs as can be observed by the band bending in Fig. 5. The dominant experimental absorption peak corresponds to the LH1 to LH2 transition (see Fig. 5) which as can be observed in

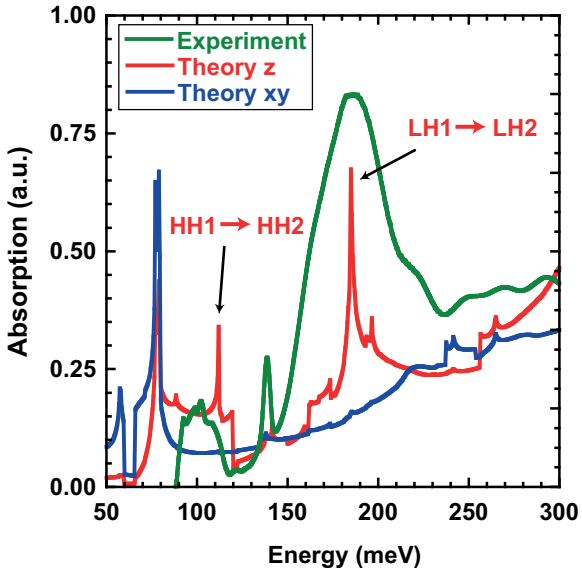

FIG. 4. The absorption for the 5.2 nm Ge QW with 3.5 nm $Si_{0.5}Ge_{0.5}$ barriers grown on a relaxed $Si_{0.2}Ge_{0.8}$ substrate at 300 K. The green curve is the experimental data from Gallacher et al.[7] at 300 K.

Fig. 4 is z-polarized as is the weaker HH1 to HH2 transition that is around 110 meV. As there are no strong xy-polarized transitions across the measured range, the weaker z-polarized modes are detected due to scattering from the heterolayers and substrate allowing z-polarised states to be observed even in the surface normal measurement configuration.[7] There is no broadening added to the modelling so it is clear that there are broadening mechanisms that have to be accounted for to accurately produce the experimental linewidth. The high doping density of 2×10^{18} cm^{-3} along with interface roughness scattering and scattering of the surface normal illumination from the back of the substrate can all increase the observed linewidth. The narrow peak close to 140 meV is related to the Si-O bond molecular absorption line in the Czochralski Si substrate[51] which is observed in all of the samples at the identical energy.

The subband spacing for this narrowest QW has the LH1 state directly above the HH1 ground state. This is

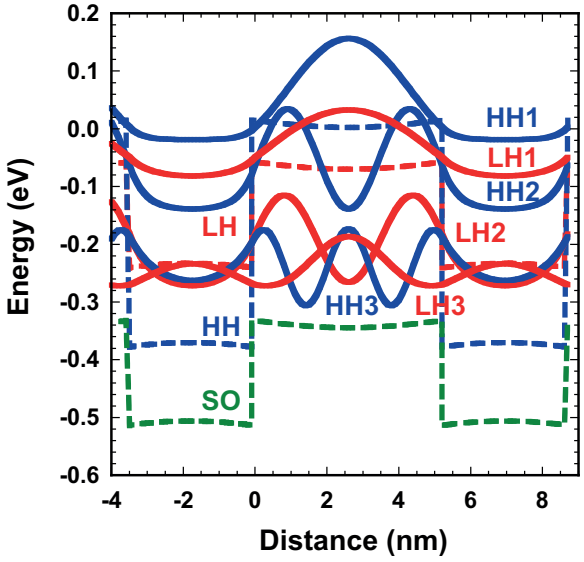

FIG. 5. The bands for the 5.2 nm Ge QW with 3.5 nm $Si_{0.5}Ge_{0.5}$ barriers grown on a relaxed $Si_{0.2}Ge_{0.8}$ substrate at 300 K. The blue lines are HH states, the red lines are LH states and the SO band is in green. The Fermi energy is set to 0 eV. The dashes are the valence band edges whilst the solid lines are the subband states.

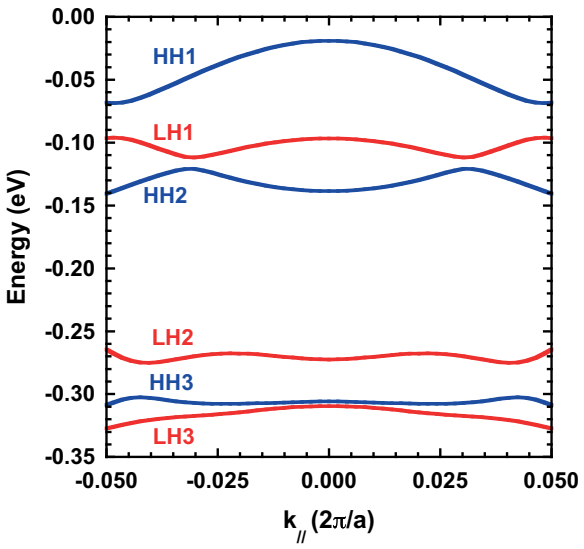

FIG. 6. The valence band dispersion for the 5.2 nm Ge QW with 3.5 nm $Si_{0.5}Ge_{0.5}$ barriers grown on a relaxed $Si_{0.2}Ge_{0.8}$ substrate at 300 K.

the only sample in which this occurs and the wider QW samples all have the HH2 directly above the HH1 with the LH1 state higher in hole energy. Figure 6 demonstrates the calculate $k_{||}$ energy dispersion for the main subband states up to the $0.05 \times \frac{2\pi}{a}$ value which was used to calculate the absorption. All of the dispersions are highly non-parabolic as has previously been reported for the valence band in the SiGe[6,18,52] and other materials system[53,54] when high levels of strain are present. The

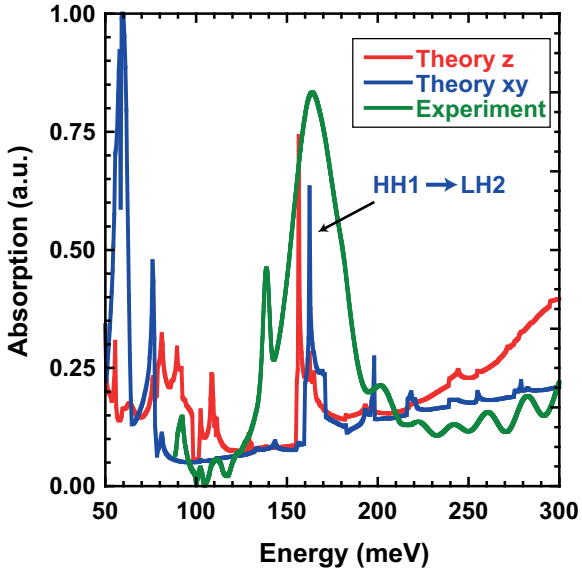

FIG. 7. The absorption for the 8.0 nm Ge QW with 5.2 nm $Si_{0.5}Ge_{0.5}$ barriers grown on a relaxed $Si_{0.2}Ge_{0.8}$ substrate. The green curve is the experimental data from Gallacher et al.[7] at 300 K.

biaxial compressive strain in the xy-plane of the QWs is 0.876% with the barriers tensile at 0.642% to balance which are significant but not as high as in a range of other reported designs.[55] It should also be pointed out that many of these subbands are not pure HH or LH states as has been previously reported but a mixture of states which can also increase the non-parabolicity.[20,52] Whilst non-parabolicity will relax the polarization selection rules, in the present work there are no transitions strong enough to allow this to be observed in the experimental range being investigated. Further work is required using polarizers along with both surface-normal and waveguide geometry measurements to test for any relaxation of the selection rules through non-parabolicity from the mixing of states with $k_{||} \neq 0$.

Figure 5 also demonstrates that the lowest hole energy continuum state is what has been marked LH3. For all the designs in this work the LH band edge is lower in hole energy than the HH band edge by over 100 meV. Also since the effective mass of the LH states are 0.0438 m_0 in the QW and 0.0984 m_0 in the barriers, the LH wavefunctions easily expand into the barriers and once the continuum states are reached provide a good mechanism for hole transport. The HH states have the heavier masses of 0.2841 m_0 in the QW and 0.4106 m_0 in the barrier and so the LH states are preferable for good hole transport especially in the barriers where the LH states are the ground state due to the tensile strain.

For the sample with the 8.1 ± 0.5 nm Ge QW with 5.2 ±0.6 nm $Si_{0.5}Ge_{0.5}$ barriers all strain symmetrized to a $Si_{0.2}Ge_{0.8}$ relaxed buffer, the modelling using 8.0 nm for the Ge QW and 5.2 nm for the $Si_{0.5}Ge_{0.5}$ barriers is presented in Fig. 7 with the corresponding bands and

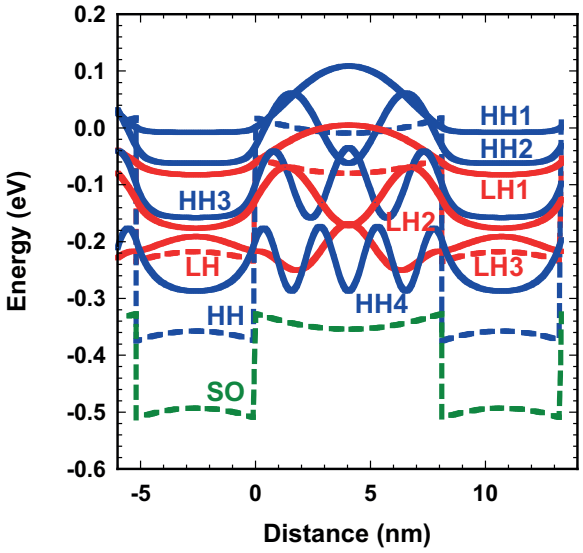

FIG. 8. The calculated valence band edges and subband states for the 8.0 nm Ge QW with 5.2 nm $Si_{0.5}Ge_{0.5}$ barriers grown on a relaxed $Si_{0.2}Ge_{0.8}$ substrate. The green curve is the experimental data from Gallacher et al.[7] at 300 K. The blue lines are HH states, the red lines are LH states and the SO band is in green. The dashes are the valence band edges whilst the solid lines are the subband states.

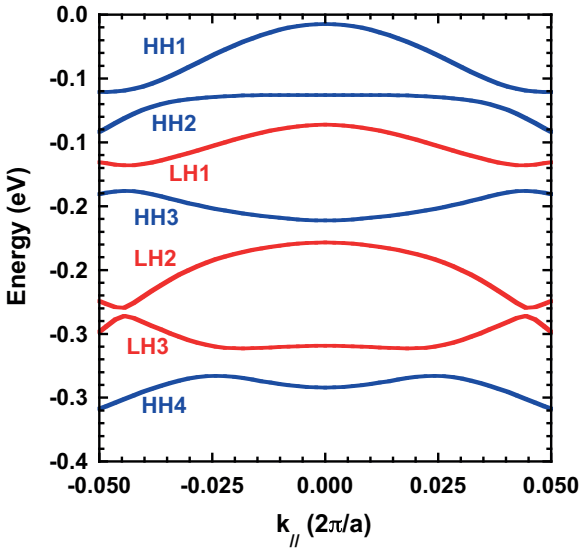

FIG. 9. The valence band dispersion for the 8.0 nm Ge QW with 5.2 nm $Si_{0.5}Ge_{0.5}$ barriers grown on a relaxed $Si_{0.2}Ge_{0.8}$ substrate.

subbands in Fig. 8. The dominant absorption peak at about 165 meV is the HH1 to LH2 transition which is xy-polarized. Unlike the 5.4 nm Ge QW sample where a z-polarized transition was observed since there were no strong xy-polarized transitions in the measurement range, only xy-polarized transitions can easily be observed in the experimental data due to the measurement geometry. The HH1 to LH1 transition is below the range

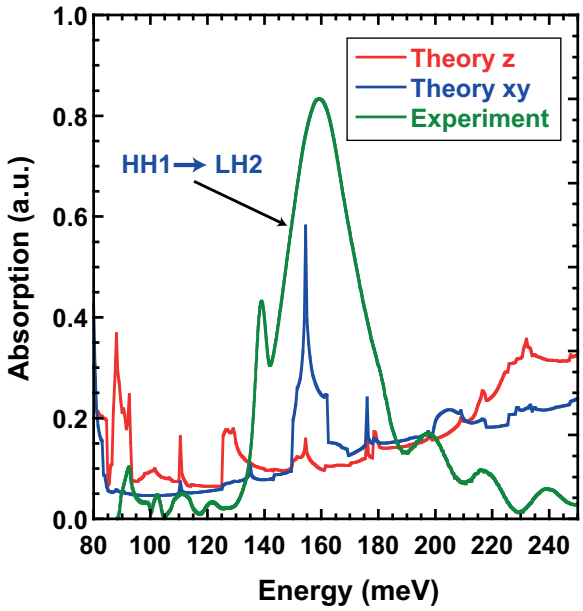

FIG. 10. The absorption for the 8.8 nm Ge QW with 5.9 nm $Si_{0.5}Ge_{0.5}$ barriers grown on a relaxed $Si_{0.2}Ge_{0.8}$ substrate. The green curve is the experimental data from Gallacher et al.[7] at 300 K.

of the mercury cadmium telluride (MCT) detector used in the experiments so only the single HH1 to LH2 transition is clearly resolved. Figure 9 presents the $k_{||}$ dispersions for the key subbands for the optical transitions. Again the energy dispersions are highly non-parabolic /colorred from the band mixing resulting in a relaxation of the parabolic selection rules. Some of the z-polarized peaks at low energy may be a signature of this relaxation but the absorption is very weak and too close to the noise level to provide certain identification of the absorption transitions. Further experiments with polarisers and longer wavelength detectors are required to confirm these transitions.

The largest QW was reported from TEM measurements as 9.2 ± 0.6 nm wide with 6.1 ± 0.6 nm $Si_{0.5}Ge_{0.5}$ barriers also on a relaxed $Si_{0.2}Ge_{0.8}$ substrate. To provide an accurate fit to the experimental absorption (Fig. 10), the QW was set to 8.8 nm and the barriers to 5.9 nm which are both inside the uncertainty of the heterolayer thicknesses. The dominant absorption peak in Fig. 10 can also be assigned to the HH1 to LH2 transition with xy-polarization when compared to subband states in Fig. 11. From the wider QW materials it is clear that the z-polarized states can only be observed if there are no stronger xy-polarized states available for absorption.

While the expected behaviour of longer wavelength absorption was achieved as the width of the QW was increased, the above modelling now explains that the observed transitions are only the same for the two widest QWs. For these the HH1 to LH2 transition is the dominant transition and the wider QWs should have xy-polarized absorption. No polarisers were used in the

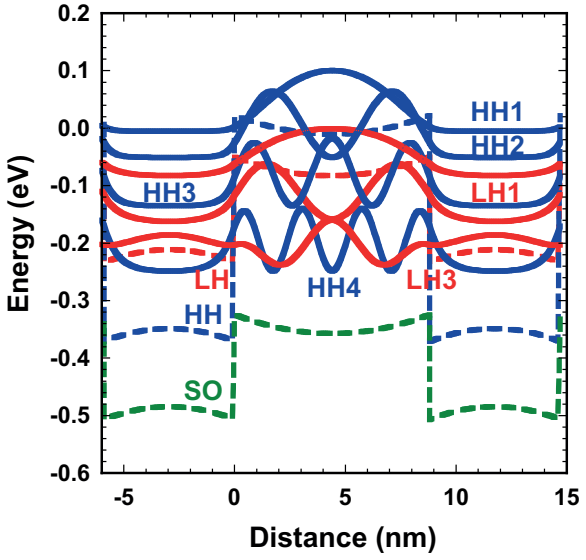

FIG. 11. The bands for the 8.8 nm Ge QW with 5.9 nm $Si_{0.5}Ge_{0.5}$ barriers grown on a relaxed $Si_{0.2}Ge_{0.8}$ substrate. The green curve is the experimental data from Gallacher et al.[7] at 300 K. The blue lines are HH states, the red lines are LH states and the SO band is in green. The dashes are the valence band edges whilst the solid lines are the subband states.

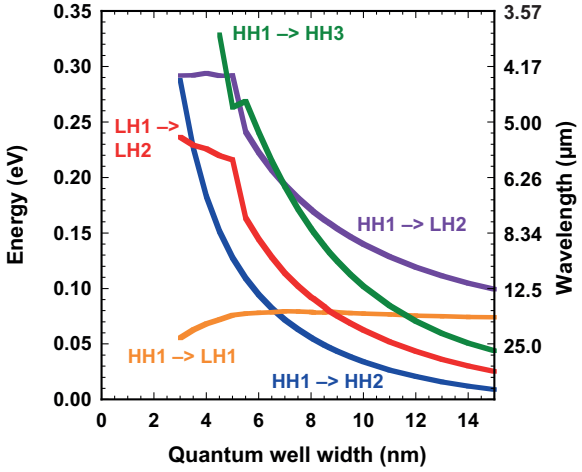

FIG. 12. The transition energies for the absorption transitions between different subband states as a function of Ge QW width at 300 K. The $Si_{0.5}Ge_{0.5}$ barrier width has been set at 0.65 times the Ge QW width to maintain strain symmetrized structures on relaxed $Si_{0.2}Ge_{0.2}$ virtual substrates.

experiments[7] to confirm the polarization but the agreement with theory for the peak positions combined with the surface-normal measurement geometry in the experiments strongly suggests zy-polarized absorption. For the narrowest QW sample, the modelling indicates that LH1 to LH2 and HH1 to HH2 are the observed transitions. Hence the reason for the narrowest QW being at the shortest wavelength (highest energy) is related not just to the increasing energy of the subband states but also to a different transitions and polarization being observed by the experiment. The experimental spectra were not calibrated so the relative amplitudes of the absorption from the 3 QW widths were not measured. The theory suggests that the xy-polarized absorption should be far stronger due to the measurement geometry but this requires further experimental measurements to confirm the prediction.

VI. ABSORPTION VERSUS QUANTUM WELL WIDTH

It is useful to investigate all the transitions as a function of QW width to understand how to design devices for different wavelengths of operation. Modelling was undertaken at 0.5 nm QW width steps between 2.0 and 15.0 nm and the resulting transitions plotted with the barrier width fixed at 0.65 times the QW width to maintain strain symmetrization throughout all the structures modelled. Figure 12 presents the main intersubband optical transitions for both polarizations as a function of the quantum well width. As can be observed from Figs. 5, 8 and 11, the HH valence band discontinunity between the Ge QW and the $Si_{0.5}Ge_{0.5}$ barriers is 393 meV, between the LH valence band edges is 183 meV and from the HH in the Ge QW to the LH in the $Si_{0.5}Ge_{0.5}$ barriers is 253 meV. The LH2 state become unconfined and this can be observed for the 5 nm wide QW with both the HH1 to LH2 and the LH1 to LH2 transitions indicating that the LH2 has moved to the continuum out of the well. A 5 nm Ge QW device would therefore operate as a z-polarized bound-to-continuum QWIP[4] detecting at 225 meV (5.5 μm wavelength) and also as a xy-polarized bound-to-continuum QWIP detecting at 291 meV (4.3 μm wavelength). All the band structure figures (Figs. 5, 8 and 11) have been plotted so the Fermi energy is set at 0 eV in the figures. Therefore for all the QW widths, Figs. 5, 8 and 11 indicate that only the HH1 state is populated with carriers at low temperatures as required for QWIP devices.

The present modelling indicates that designs of bound-to-continuum QWIPs using Ge QWs at other wavelengths requires the change in Ge content in the barriers and the substrates to produce absorption at other energies (wavelengths). By increasing the Ge content in the barriers and the relaxed virtual substrate then bound-to-continuum QWIPs can be produced with z-polarization above 5.5 μm wavelength and xy-polarized bound-to-continuum QWIP longer than 4.3 μm wavelength. To achieve Ge QW QWIPs with shorter wavelength absorption will require lower Ge content barriers and relaxed virtual substrates.

VII. CONCLUSIONS

The parameters to run an 8-band **k**.**p**-theory band structure tool have been derived including the direct bandgap coupling between the valence band and the conduction band for Si and Ge. The tool with these parameters was used to model mid-infrared intersubband transitions for a range of Ge QWs grown with $Si_{0.5}Ge_{0.5}$ barriers on a relaxed buffer of $Si_{0.2}Ge_{0.8}$. The modelling results demonstrate that the direct band coupling is essential to accurately model the optical absorption of intersubband transitions of p-type Ge QWs. A range of bowing parameters have also been derived for the band structure modelling and demonstrated to be required to achieve accurate results. Changing the Ge QW width resulted in a change in the subband transitions being observed as well as the polarization of the absorption. The work also suggests the Ge compositions required for designs of Ge QWIPs for a range of mid-infrared wavelengths.

VIII. ACKNOWLEDGEMENTS

The research leading to these results has received funding from the European Union's 7^{th} Framework Programme through the GEMINI project (Project No. 613055) and the U.K. EPSRC (Project No. EP/N003225/1). The author would also like to acknowledge useful discussions with P. Biagioni, M. Ortolani, G. Isella, D. Brida, J. Frigerio, A. Ballabio, R.W. Millar, K. Gallacher, A. Bashir and I. MacLaren.

[1] A. Rogalski, J. Appl. Phys. **93**, 4355 (2003).
[2] L. Baldassarre, E. Sakat, J. Frigerio, A. Samarelli, K. Gallacher, E. Calandrini, G. Isella, D. J. Paul, M. Ortolani, and P. Biagioni, Nano Lett. **15**, 7225 (2015).
[3] A. Rogalski, Infrared Phys. Technol. **38**, 295 (1997).
[4] B. F. Levine, J. Appl. Phys. **74**, R1 (1993).
[5] D. J. Paul, Elec. Lett. **45**, 582 (2009).
[6] D. J. Paul, Laser & Photon. Rev. **4**, 610 (2010).
[7] K. Gallacher, A. Ballabio, R. W. Millar, J. Frigerio, A. Bashir, I. MacLaren, G. Isella, M. Ortolani, and D. J. Paul, Appl. Phys. Lett. **108**, 091114 (2016).
[8] R. Soref, Nat Photon **4**, 495 (2010).
[9] R. P. G. Karunasiri, J. S. Park, Y. J. Mii, and K. L. Wang, Appl. Phys. Lett. **57**, 2585 (1990).
[10] J. S. Park, T. L. Lin, E. W. Jones, H. M. D. Castillo, and S. D. Gunapala, Appl. Phys. Lett. **64**, 2370 (1994).
[11] P. Kruck, M. Helm, T. Fromherz, G. Bauer, J. F. Nützel, and G. Abstreiter, Appl. Phys. Lett. **69**, 3372 (1996).
[12] D. J. Paul, Semicond. Sci. Technol. **19**, R75 (2004).
[13] M. M. Rieger and P. Vogl, Phys. Rev. B **48**, 14276 (1993).
[14] M. V. Fischetti and S. E. Laux, J. Appl. Phys. **80**, 2234 (1996).
[15] M. Bonfanti, E. Grilli, M. Guzzi, M. Virgilio, G. Grosso, D. Chrastina, G. Isella, H. von Känel, and A. Neels, Phys. Rev. B **78**, 041407 (2008).
[16] Z. Ikonić, P. Harrison, and R. W. Kelsall, Phys. Rev. B **64**, 245311 (2001).
[17] M. El Kurdi, G. Fishman, S. Sauvage, and P. Boucaud, J. Appl. Phys. **107**, 013710 (2010).
[18] D. J. Paul, Phys. Rev. B **77**, 155323 (2008).
[19] T. Fromherz, E. Koppensteiner, M. Helm, G. Bauer, J. F. Nützel, and G. Abstreiter, Phys. Rev. B **50**, 15073 (1994).
[20] T. Fromherz, M. Meduňa, G. Bauer, A. Borak, C. V. Falub, S. Tsujino, H. Sigg, and D. Grützmacher, J. Appl. Phys. **98**, 044501 (2005).
[21] S. Tsujino, A. Borak, C. Falub, T. Fromherz, L. Diehl, H. Sigg, and D. Grützmacher, Phys. Rev. B **72**, 153315 (2005).
[22] R. W. Kelsall, Z. Ikonic, P. Murzyn, C. R. Pidgeon, P. J. Phillips, D. Carder, P. Harrison, S. A. Lynch, P. Townsend, D. J. Paul, S. L. Liew, D. J. Norris, and A. G. Cullis, Phys. Rev. B **71**, 115326 (2005).
[23] S. A. Lynch, D. J. Paul, P. Townsend, G. Matmon, Z. Suet, R. W. Kelsall, Z. Ikonic, P. Harrison, J. Zhang, D. J. Norris, A. G. Cullis, C. R. Pidgeon, P. Murzyn, B. Murdin, M. Bain, H. S. Gamble, M. Zhao, and W.-X. Ni, IEEE J. Select Topics Quant. Elec. **12**, 1570 (2006).
[24] M. Califano, N. Q. Vinh, P. J. Phillips, Z. Ikonić, R. W. Kelsall, P. Harrison, C. R. Pidgeon, B. N. Murdin, D. J. Paul, P. Townsend, J. Zhang, I. M. Ross, and A. G. Cullis, Phys. Rev. B **75**, 045338 (2007).
[25] R. Winkler, M. Merkler, T. Darnhofer, and U. Rössler, Phys. Rev. B **53**, 10858 (1996).
[26] Landolt-Börnstein, ed., *Band 17 Halbleiter* (Springer-Verlag, Berlin, 1982).
[27] P. Lawaetz, Phys. Rev. B **4**, 3460 (1971).
[28] S. Birner, "Nextnano++," (2016).
[29] T. Eissfeller, *Linear Optical Response of Semiconductor Nanodevices*, Ph.D. thesis, Physics Department, Technische Universität München (2008).
[30] S. Birner, *Modelling of semiconductor nanostructures and semiconductor-electrolyte interfaces*, Ph.D. thesis, Walter Schottky Institute, Technische Universität München (2011).
[31] D. De Salvador, M. Petrovich, M. Berti, F. Romanato, E. Napolitani, A. Drigo, J. Stangl, S. Zerlauth, M. Mühlberger, F. Schäffler, G. Bauer, and P. C. Kelires, Phys. Rev. B **61**, 13005 (2000).
[32] J. P. Dismukes, L. Ekstrom, and R. J. Paff, J. Phys. Chem. **68**, 3021 (1964).
[33] Y. P. Varshni, Physica **34**, 149 (1967).
[34] C. G. Van de Walle, Phys. Rev. B **39**, 1871 (1989).
[35] J. Weber and M. I. Alonso, Phys. Rev. B **40**, 5683 (1989).
[36] L. D. Laude, F. H. Pollak, and M. Cardona, Phys. Rev. B **3**, 2623 (1971).
[37] M. Chandrasekhar and F. H. Pollak, Phys. Rev. B **15**, 2127 (1977).
[38] S.-H. Wei and A. Zunger, Phys. Rev. B **60**, 5404 (1999).
[39] C. G. Van de Walle and R. M. Martin, Phys. Rev. B **34**, 5621 (1986).
[40] G. Dresselhaus, A. F. Kip, and C. Kittel, Phys. Rev. **98**, 368 (1955).
[41] J. M. Luttinger, Phys. Rev. **102**, 1030 (1956).
[42] B. A. Foreman, Phys. Rev. B **48**, 4964 (1993).
[43] B. A. Foreman, Phys. Rev. B **56**, R12748 (1997).
[44] J. A. Van Vechten, Phys. Rev. **187**, 1007 (1969).
[45] J. C. Hensel and K. Suzuki, Phys. Rev. B **9**, 4219 (1974).
[46] P. Y. Yu and M. Cardona, *Fundamentals of Semiconductors: Physics and Material Properties*, edited by 3^{rd} (Springer-Verlag, 2001).
[47] J. Los, A. Fasolino, and A. Catellani, Phys. Rev. B **53**, 4630 (1996).
[48] J. P. Loehr, Phys. Rev. B **52**, 2374 (1995).
[49] P. Boucaud, L. Wu, F. Julien, J.-M. Lourtioz, I. Sagnes, Y. Campidelli, and P.-A. Badox, Appl. Surf. Sci. **102**, 342 (1996).
[50] P. Kruck, A. Weichselbaum, M. Helm, T. Fromherz, G. Bauer, J. Nützel, and G. Abstreiter, Superlat. Microstruc. **23**, 61 (1998).
[51] R. C. Newman, J. Phys.: Conden. Matter **12**, R335 (2000).
[52] F. Bottegoni, A. Ferrari, G. Isella, M. Finazzi, and F. Ciccacci, Phys. Rev. B **85**, 245312 (2012).
[53] S. W. Corzine, R. H. Yan, and L. A. Coldren, Appl. Phys. Lett. **57**, 2835 (1990).

[54]F. Dujardin, N. Marréaud, and J. Laurenti, Solid State Comm. **98**, 297 (1996).

[55]G. Matmon, D. J. Paul, L. Lever, M. Califano, Z. Ikonić, R. W. Kelsall, J. Zhang, D. Chrastina, G. Isella, H. von Känel, E. Müller, and A. Neels, J. Appl. Phys. **107**, 053109 (2010).